



Cite this: *Nanoscale*, 2018, **10**, 21748

## Low-defectiveness exfoliation of MoS<sub>2</sub> nanoparticles and their embedment in hybrid light-emitting polymer nanofibers†

Alberto Portone,<sup>a,b</sup> Luigi Romano,<sup>a,b</sup> Vito Fasano,<sup>a</sup> Riccardo Di Corato,<sup>b</sup> Andrea Camposeo,<sup>b</sup> Filippo Fabbri,<sup>d</sup> Francesco Cardarelli,<sup>e</sup> Dario Pisignano<sup>b,f</sup> and Luana Persano<sup>b</sup>

Molybdenum disulfide (MoS<sub>2</sub>) has been attracting extraordinary attention for its intriguing optical, electronic and mechanical properties. Here, we demonstrate hybrid, organic–inorganic light-emitting nanofibers based on MoS<sub>2</sub> nanoparticle dopants obtained through a simple and inexpensive sonication process in *N*-methyl-2-pyrrolidone and successfully encapsulate the nanofibers in polymer filaments. The gentle exfoliation method used to produce the MoS<sub>2</sub> nanoparticles results in low defectiveness and preserves the stoichiometry. The fabricated hybrid fibers are smooth, uniform and flawless and exhibit bright and continuous light emission. Moreover, the fibers show significant capability for waveguiding self-emitted light along their longitudinal axes. These findings suggest that emissive MoS<sub>2</sub> fibers formed by gentle exfoliation are novel and highly promising optical materials for sensing surfaces and photonic circuits.

Received 5th August 2018,  
Accepted 12th October 2018

DOI: 10.1039/c8nr06294c

rsc.li/nanoscale

### 1. Introduction

Layered molybdenum disulfide (MoS<sub>2</sub>)<sup>1–4</sup> is a quasi-two-dimensional material with covalent in-plane bonds and weak out-of-plane van der Waals interactions. Such transition metal dichalcogenides show highly interesting semiconducting properties,<sup>5</sup> including sizable direct band gap (1.2–2.2 eV),<sup>2,6,7</sup> and can be easily intercalated, making them potentially useful for a variety of electronic applications.<sup>3,8,9</sup> MoS<sub>2</sub> nanoparticles (NPs) isolated or interspersed within flakes show quantum confinement effects, with a blue-shift in photoluminescence (PL) upon crystal size reduction,<sup>7,10</sup> along with excitation-dependent PL emission.<sup>10,11</sup> Combined with the potentially improved brightness compared to mono- and few-layered

forms,<sup>7</sup> these properties, make MoS<sub>2</sub> NPs highly attractive for the realization of tunable light sources and optical sensors.

Embedding such materials in hybrid polymer architectures such as microspheres or fibers would offer additional advantages, including the easier manipulation of functional NPs, their integration in flexible optoelectronic components, and improved stability.<sup>12–15</sup> For instance, fibers with diameters up to few micrometers, which can be straightforwardly electrospun by intense electric fields (0.01–0.1 MV m<sup>−1</sup>) applied to NP–polymer solutions with sufficient degrees of entanglement,<sup>16–18</sup> would make MoS<sub>2</sub> dopants utilizable in photonic circuits and boards, including arrays of optical sensors and synaptic components.<sup>19,20</sup> The process is highly versatile once proper dispersion conditions are found for NPs, leading to either individual filaments or large-area mats consisting of long and flexible fibers. In previous works, both hybrid and single-component light-emitting materials showed quantum yields higher than those of corresponding conjugated polymer films along with chain alignment and optical anisotropy.<sup>21–23</sup> In addition, electrostatically interacting molecular systems with intercoupled optomechanical properties have been demonstrated.<sup>24</sup> The encapsulation of MoS<sub>2</sub> flakes in carbon fibers has been explored as a strategy to realize anodes for high-performance batteries.<sup>25,26</sup> However, the emission properties of these compounds in polymer nanofibers and their application in prototypical photonic components have not been studied.

<sup>a</sup>Dipartimento di Matematica e Fisica 'Ennio De Giorgi', Università del Salento, via Arnesano, I-73100 Lecce, Italy

<sup>b</sup>NEST, Istituto Nanoscienze-CNR, Piazza San Silvestro 12, I-56127 Pisa, Italy. E-mail: luana.persano@nano.cnr.it

<sup>c</sup>Center for Biomolecular Nanotechnologies (CBN), Istituto Italiano di Tecnologia, Via Barsanti, I-73010 Arnesano (LE), Italy

<sup>d</sup>Center for Nanotechnology Innovation @NEST, Istituto Italiano di Tecnologia, Piazza San Silvestro 12, I-56127 Pisa, Italy

<sup>e</sup>NEST, Scuola Normale Superiore, Piazza San Silvestro 12, I-56127 Pisa, Italy

<sup>f</sup>Dipartimento di Fisica, Università di Pisa, Largo B. Pontecorvo 3, I-56127 Pisa, Italy. E-mail: dario.pisignano@unipi.it

†Electronic supplementary information (ESI) available: Full experimental details, EDS data, further absorption and micro-Raman characterization, and the dimensional distribution of realized fibers. See DOI: 10.1039/c8nr06294c



Focusing on optical properties, in this study, we introduce light-emitting fibers based on MoS<sub>2</sub> NPs interspersed in flakes and electrospun jointly with a poly(methyl methacrylate) (PMMA) matrix. The NPs are obtained through gentle exfoliation, which is found to reduce the MoS<sub>2</sub> particle size in all three spatial dimensions while preserving the low defect concentration and stoichiometry, as highlighted by micro-Raman mapping. The resulting fibers have smooth surfaces, exhibit uniform and bright broadband emission, and are capable of guiding generated light along their length. Thus, the fibers represent a novel hybrid material that can be promptly utilized to build optical circuits based on miniaturized waveguides and integrated sensing regions.

## 2. Experimental methods

MoS<sub>2</sub> NPs were produced *via* the exfoliation of the bulk powder (Aldrich, particle size <2 μm) by ultrasonication for 8 h in *N*-methyl-2-pyrrolidone (NMP). Following the sonication step, centrifugation at 1000 rpm was carried out for 45 min to remove bulk residues and collect the supernatant. The resulting particles were inspected optically by confocal and UV-Vis spectroscopy, and morphologically by scanning electron microscopy (SEM) and transmission electron microscopy (TEM), and chemically by energy-dispersive X-ray spectrometry (EDS).

Confocal analysis was performed on vacuum-dried drops (50 μL) cast from the achieved dispersion, placed onto a glass substrate and excited with a cw laser at wavelength  $\lambda = 488$  nm. Micro-Raman experiments were carried out using a Renishaw InVia spectrometer equipped with a confocal optical microscope and a 532 nm excitation laser. PL lifetime measurements were performed in confocal mode by exciting light-emitting fibers with a 470 nm pulsed diode laser at 40 MHz. Signals were collected by a time-correlated single-photon counting setup. Full details on the experimental methods, including the realization of electrospun hybrid fibers, are reported in the ESI.†

## 3. Results and discussion

We produced MoS<sub>2</sub> NPs by exfoliating the bulk powder *via* ultrasonication in NMP and subsequent centrifugation. The high surface tension of NMP (40 mJ m<sup>-2</sup>), which roughly matches the estimated surface energy of few-layered MoS<sub>2</sub> (46.5 mJ m<sup>-2</sup>), allows a stable dispersion to be obtained.<sup>27–30</sup> In addition, the exfoliation process is simple and environmentally friendly. The process is driven by sonochemical cavitation phenomena *via* the formation and implosive collapse of gas bubbles. The resulting increase in local temperature and pressure favors exfoliation and eventually lead to the formation of nanosized particles.

Representative SEM images of the obtained MoS<sub>2</sub> samples covered by few-nm-thick metal layers to facilitate inspection

are shown in Fig. 1a. The images show layered flakes with transverse sizes up to a few micrometers and decorated with 20–80 nm particles (inset of Fig. 1a). The elemental compositions of both the flakes and particles were evaluated by EDS (Fig. S1 in the ESI†) and are highlighted by a sharp and intense peak at 2.3 keV, which is attributed to the presence of the transition metal dichalcogenide.<sup>31,32</sup>

The PL emission from cast samples appears in the form of bright spots (Fig. 1b) with a maximum intensity at 550 nm and full width at half maximum (FWHM) of 56 nm. These characteristics are typical of the fluorescence spectrum of MoS<sub>2</sub> particles with nm-scale lateral dimensions.<sup>7,11,33</sup> Indeed, the formation of small fragments during sonication is generally associated with a blue-shift in emission around 450–600 nm,

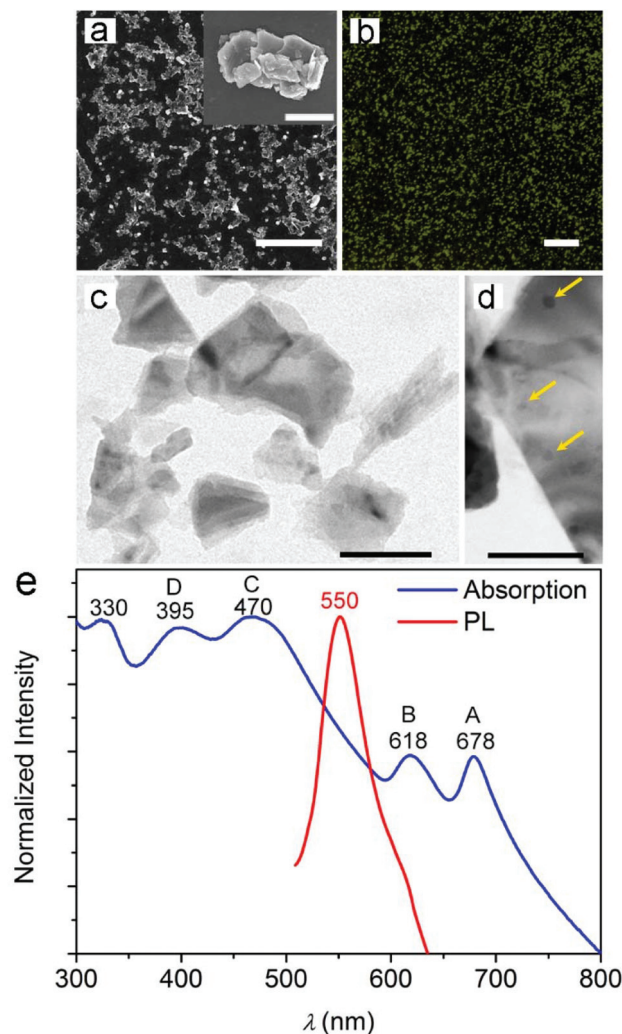


**Fig. 1** (a) SEM micrograph of MoS<sub>2</sub> particles following exfoliation. Scale bar = 5 μm. The inset shows a representative single aggregate of particles at higher magnification. Scale bar = 1 μm. (b) Confocal fluorescence micrograph of a drop-cast MoS<sub>2</sub> dispersion. Scale bar = 10 μm. (c, d) TEM micrographs of MoS<sub>2</sub> following exfoliation. MoS<sub>2</sub> NPs with diameters down to 10 nm are highlighted by yellow arrows. Scale bar = 100 nm (c) and 50 nm (d), respectively. (e) Absorbance (blue line) and PL emission spectra (red line) of the MoS<sub>2</sub> dispersion.



depending on the lateral size of the formed fragments and on the excitation wavelength. Upon excitation at 488 nm, the PL peak at 550 nm can be attributed to MoS<sub>2</sub> NPs with lateral dimensions up to a few tens of nm.<sup>7,10,11,33</sup> This is also supported by the TEM images shown in Fig. 1c and d, which provide evidence for the formation of few-layered MoS<sub>2</sub> flakes and show almost round-shaped NPs with diameters down to 10 nm.

To investigate the properties of the NPs more in depth, we measured the UV-Vis absorption spectra of the liquid dispersion of MoS<sub>2</sub> after centrifugation. The absorbance spectrum (Fig. 1e) shows characteristic features of MoS<sub>2</sub> NPs and nanosheets, with two peaks between 600 and 700 nm and a broad band with two peaks at 395 and 470 nm.<sup>10,34</sup> The two low-energy absorption peaks (A and B in Fig. 1e) are known to correspond to excitonic transitions and occur between the splitted valence bands and the conductance band at the K-point of the Brillouin zone of MoS<sub>2</sub> nanosheets.<sup>7</sup> The measured extinction coefficient at 678 nm is 412 mL mg<sup>-1</sup> m<sup>-1</sup> (Fig. S2†). Through quasiparticle self-consistent GW calculations, energy differences between the splitted valence bands of 146 and 174 meV have been predicted for MoS<sub>2</sub> monolayers and bilayers, respectively, due to spin-orbit coupling and inter-layer interaction.<sup>35</sup> Here, the energy gap of about 175 meV between the A and B transitions is therefore consistent with the formation of few-layered flakes. Additional absorption peaks at 470 nm (C in Fig. 1e) and 395 nm (D) are regarded to be associated with transitions involving other regions with high density of state,<sup>36–38</sup> as from the deep valence band to the conduction band.<sup>10,39</sup> On the whole, peaks A–D are typical features of exfoliated MoS<sub>2</sub>. Moreover, an absorption peak in the UV spectrum (at about 330 nm) can be clearly seen in Fig. 1e. This peak is attributed to the formation of NPs with small sizes in the dispersion and consequent quantum confinement effects.<sup>7,10,11,39</sup> These results are collectively in agreement with previous findings suggesting how exfoliation procedures might lead to complex dispersions of heterodimensional MoS<sub>2</sub> nanostructures.

The effects of the ultrasonication process on the MoS<sub>2</sub> bulk powder can be better analyzed by Raman spectroscopy. Fig. 2a compares the Raman spectra of the MoS<sub>2</sub> pristine powder (blue line) and the NPs after the exfoliation process (red line). Both spectra exhibit two peaks: the E<sub>2g</sub> peak corresponding to the in-plane vibrational mode and the A<sub>1g</sub> peak related to the out-of-plane vibrational mode.

The MoS<sub>2</sub> pristine powder shows the characteristic E<sub>2g</sub> and A<sub>1g</sub> Raman modes at 376.8 and 403.2 cm<sup>-1</sup>, respectively. The corresponding vibrational modes in the exfoliated MoS<sub>2</sub> nanocrystals are shifted up to 381.6 and 406.8 cm<sup>-1</sup>, respectively. The stiffening of the Raman modes is likely attributed to the nanoscale size of MoS<sub>2</sub> in all three spatial dimensions following the exfoliation process. Indeed, this particular effect has been previously reported for 18 nm MoS<sub>2</sub> nanocrystals.<sup>7</sup> In addition, the spectral spacing between the E<sub>2g</sub> and A<sub>1g</sub> modes (25.2 cm<sup>-1</sup>) confirms that our MoS<sub>2</sub> consist of six to 10 layers.<sup>40</sup> The pristine powder exhibits a corresponding Raman mode spacing equal to 26.4 cm<sup>-1</sup>, in agreement with the value

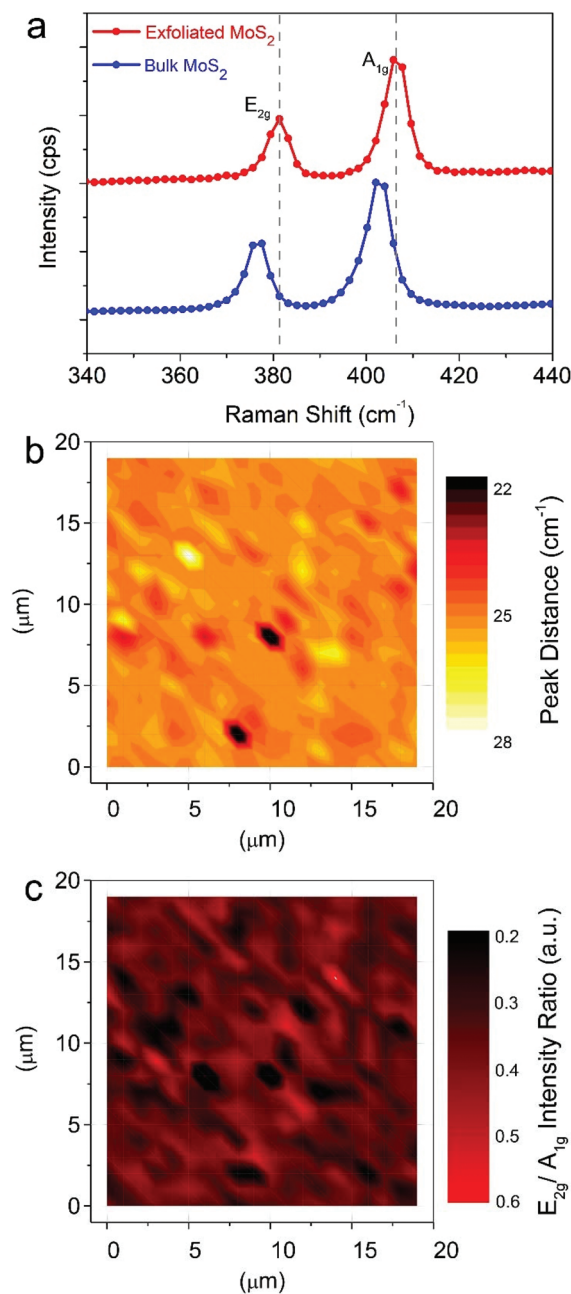


Fig. 2 (a) Raman spectra of bulk MoS<sub>2</sub> (blue spectrum) and a drop-cast MoS<sub>2</sub> dispersion after the exfoliation process (red spectrum) acquired using a 532 nm laser. The spectra are vertically shifted for clarity. (b, c) Maps of the Raman mode spacing (b) and of the E<sub>2g</sub>–A<sub>1g</sub> intensity ratio (c) acquired for the drop-cast dispersion (map size = 19 × 19 μm<sup>2</sup>).

of bulk MoS<sub>2</sub>.<sup>40</sup> Interestingly, the intensity ratio between the E<sub>2g</sub> and A<sub>1g</sub> modes, which is often employed as a benchmark of the stoichiometry and defectiveness of MoS<sub>2</sub>,<sup>41,42</sup> is similar in both spectra (~0.5). This characteristic is especially relevant for using the achieved dispersions to build light-emitting components since it highlights that the exfoliation process does not worsen the material in terms of sulfur understoichiometry<sup>42</sup> or increased defects.<sup>43</sup>



To evaluate the homogeneity of the achieved dispersion of NPs, we also carried out Raman mapping on an area of about  $360 \mu\text{m}^2$  following drop casting on a glass substrate. Fig. 2b and c show the maps of the Raman mode spacing and of the  $E_{2g}$ - $A_{1g}$  intensity ratio, respectively. Fig. S3† shows the control maps for the pristine  $\text{MoS}_2$  powder, which clearly highlight that the initial system is composed of bulk material with good homogeneity in terms of sulphur stoichiometry. In contrast, the Raman mode spacing map in Fig. 2b demonstrates that the system obtained after ultrasonication is homogeneously composed by few-layer  $\text{MoS}_2$  nanocrystals with minor bulk residues. As shown in Fig. 2c, defective areas in which the intensity ratio between the  $E_{2g}$  and  $A_{1g}$  modes is below 0.5 are very small within the intensity ratio map ( $\sim 7\%$  of the analyzed region).

Fibers embedded in the  $\text{MoS}_2$  NPs as dopants were prepared by electrospinning after dissolving the polymer matrix in a complex dispersion (see ESI† for details). The resulting hybrid fibers (Fig. 3a) are uniform with average diameters around  $1.6 \mu\text{m}$  and smooth surfaces (Fig. S4†). Confocal fluorescence imaging revealed a uniform PL intensity along the longitudinal axis of each fiber (Fig. 3b), suggesting the homogeneous incorporation of  $\text{MoS}_2$  in the filaments. This finding is further supported by the 3D reconstruction of fibers obtained

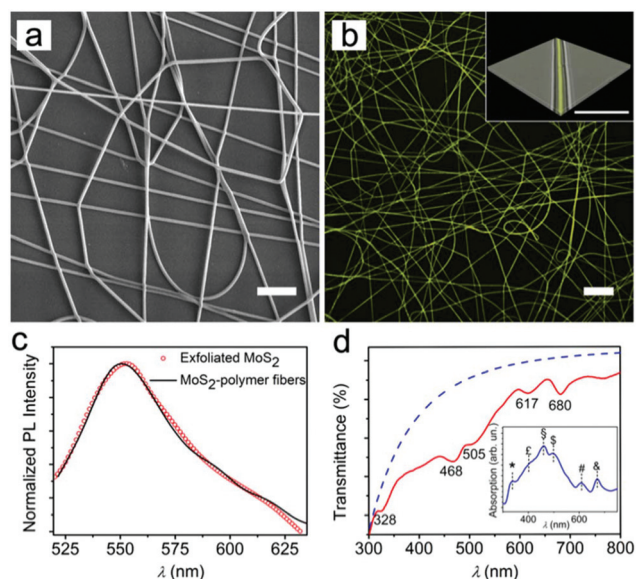
by Z-axis scanning (*i.e.*, perpendicular to the substrate on which the fibers are deposited; inset of Fig. 3b).

Fig. 3c compares the PL intensities of the achieved  $\text{MoS}_2$  particles and fibers. No significant difference in emission is observed, indicating that emission was well preserved upon electrospinning. Similarly, the absorbance spectrum (Fig. 3d) indicates that the characteristic features of  $\text{MoS}_2$  are generally well preserved in the fibers, including the UV component at about 330 nm. This allows one to conclude that the NPs are effectively embedded in the hybrid fibrous material.

In fact, reduced transmission is also indicative of remarkable light-scattering phenomena arising in the fibrous sample, which can be straightforwardly taken into account as being proportional to the  $n$ th-power of the wavelength, with  $-4 < n < -1$  (dashed line in Fig. 3d).<sup>34,37</sup> Once such a light-scattering component is considered, fiber absorption also shows features that can be ascribed to the C (at  $\sim 460$  nm) and D ( $\sim 400$  nm) transitions of  $\text{MoS}_2$  (upon more significant layering in the polymer matrix), together with an additional peak at 496 nm, which is also likely to be related to the aggregation of larger  $\text{MoS}_2$  flakes in the filaments (inset of Fig. 3d). In this respect, the polymer fibers represent an interesting environment in which the edge and quantum effects<sup>44</sup> of exfoliated two-dimensional materials can be obtained within confined volumes.

To study the PL lifetime of the  $\text{MoS}_2$ -doped fibers, we used time-correlated single-photon counting detection. The observed PL lifetime (Fig. 4a) displays a decay with an average characteristic time of  $(3.1 \pm 0.1)$  ns. This result is comparable to the values reported in previous works, in which observed lifetimes typically ranged from 1.5 to 5.9 ns.<sup>10,11,45–47</sup> The lifetime map in the inset of Fig. 4a shows a homogeneous green color along all the fibers, indicating that the average lifetime is uniform in all the filaments. Notably, the acquired data are best represented by fitting to a biexponential model with associated lifetimes of  $(1.3 \pm 0.1)$  ns and  $(4.4 \pm 0.3)$  ns and fractional contributions of 60% and 40%, respectively. The quality of the fit was assessed by the goodness of the obtained residuals (the monoexponential- and biexponential-derived residuals are reported in Fig. 4b as green dots and a blue line, respectively). Such biexponential behavior is not surprising and has been reported by others for  $\text{MoS}_2$  NPs.<sup>10,11</sup> This phenomenon might depend on the presence of different species of  $\text{MoS}_2$  nanostructures within the fibers.<sup>10</sup> In fact, heterodimensional  $\text{MoS}_2$  nanostructures present different lifetimes.<sup>45</sup>

Finally, the waveguiding features of the  $\text{MoS}_2$ -doped, light-emitting fibers were analyzed by microphotoluminescence ( $\mu$ -PL) using suspended fibers (Fig. 4c) to avoid any optical loss induced by the substrate/fiber interface. To assess the propagation losses for light emitted by  $\text{MoS}_2$  NPs and channeled along individual hybrid filaments, the intensities of PL escaping from the fiber surface and from the tip were imaged and measured as a function of the distance ( $d$ ) of the tip from the excitation spot. Fig. 4d shows a typical PL image of the fiber under excitation by a focused laser beam (red circle). The spatial decay of the self-waveguided emission is displayed in



**Fig. 3** (a) SEM micrograph of  $\text{MoS}_2$ -doped fibers. Scale bar =  $20 \mu\text{m}$ . (b) Fluorescence confocal micrograph of fibers. Scale bar =  $20 \mu\text{m}$ . The inset shows a 3D reconstruction of merged fluorescence and transmission confocal micrographs of an individual fiber by Z-axis scanning. Scale bar =  $10 \mu\text{m}$ . (c) PL emission spectra of exfoliated  $\text{MoS}_2$  drop-cast on glass (red circles) and  $\text{MoS}_2$ -polymer fibers (black line). The PL peak is at about 550 nm. (d) Transmittance spectrum of aligned fibers. The blue dashed line is the calculated scattering background ( $\sim \lambda^n$  with  $n = -3.66$ ). Inset shows the scattering background-corrected absorption spectrum. Peaks are at 336 (\*), 401 (E), 460 (§), 497 (§), 611 (#) and 673 nm (θ).



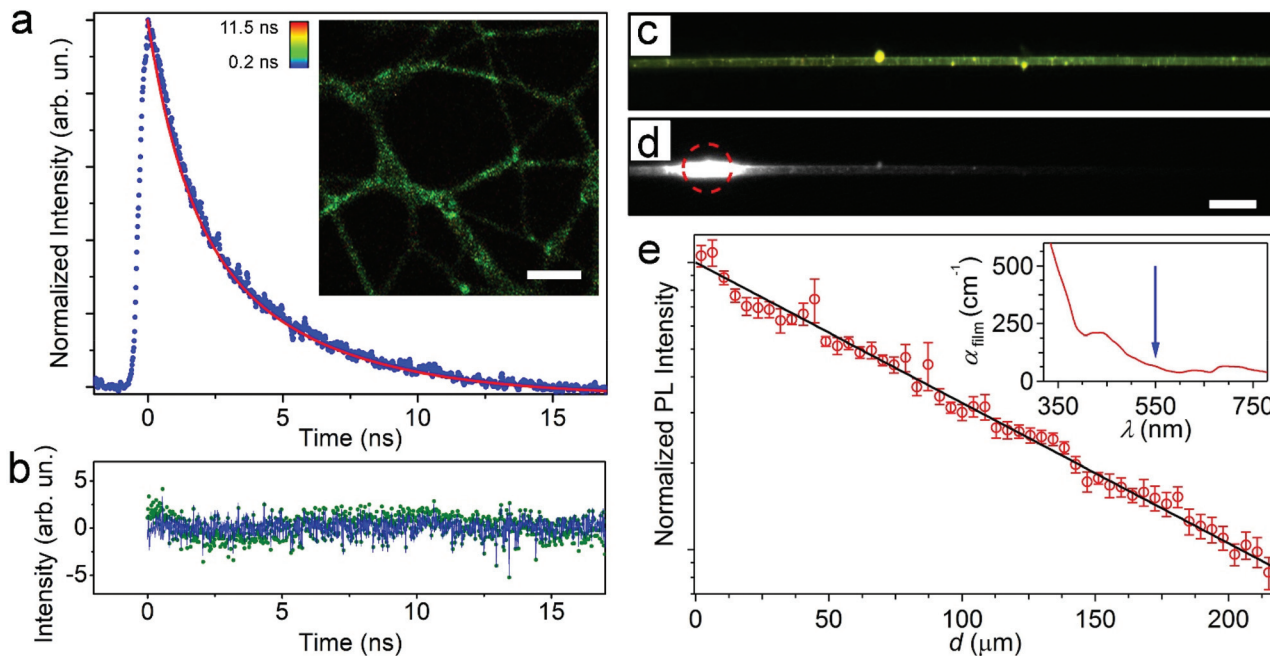


**Fig. 4** (a) Fluorescence lifetime of MoS<sub>2</sub>-doped fibers. The data are fitted using a biexponential decay model (red line). The inset shows an average lifetime map obtained by fitting the fluorescence decay curve in each pixel of the image. Scale bar = 10 μm. (b) Residuals of the monoexponential (green dots) and biexponential (blue line) fittings. (c) Fluorescence micrograph of a freestanding MoS<sub>2</sub>-doped fiber. Bright spots are associated with particle clusters. (d) PL of the same fiber during excitation by a focused laser beam (red circle in the left part of the image). Scale bar = 10 μm. (e) Spatial decay of light intensity guided inside the fiber vs. distance  $d$  from the photoexcitation spot. The continuous line is the best fit to an exponential decay according to the function  $I = I_0 e^{-\alpha d}$ . The inset shows the wavelength dependence of propagation loss in a reference film doped with MoS<sub>2</sub>. The vertical arrow highlights the analyzed emission wavelength (~550 nm).

**Fig. 4e.** The continuous line is the best fit of the experimental data by an exponential function,  $I_{PL} = I_0 \exp(-\alpha d)$ , where  $I_{PL}$  is the PL intensity,  $I_0$  is a pre-exponential factor that indicates the intensity measured at very small  $d$  values, and  $\alpha$  is the loss coefficient. The fits lead to  $\alpha = 110 \text{ cm}^{-1}$ , roughly corresponding to a light transport length of 90 μm, and losses that are significantly lower than reported for other hybrid nanofibers (e.g., those doped with CdSe quantum dots) and in line with the best values found in conjugated polymer nanofibers.<sup>48,49</sup> Theoretically, for PMMA nanofibers in air, optical losses affecting photons carried along the length of the waveguide are calculated by considering Rayleigh scattering from the nanofiber surface roughness (a few nanometers, as measured by atomic force microscopy) and are expected to be in the range  $10\text{--}100 \text{ cm}^{-1}$ .<sup>48,50</sup> The optical losses for photons carried along the hybrid fiber can be also attributed to self-absorption by the active component (i) along with light-scattering from either bulk (ii) or surface (iii) defects or inhomogeneities. The contribution of absorption from the polymer matrix to optical loss can be neglected as it is on the order of  $10^{-3}\text{--}10^{-2} \text{ cm}^{-1}$  in the visible range.<sup>51</sup>

The contributions [(i) + (ii)] of absorption and Rayleigh scattering by bulk defects, which are mainly related to the difference in refractive index between the polymer and inorganic fillers, can be determined by measuring losses for an optical beam propagating through a film of known thickness with the

same composition as the nanofibers. The inset of Fig. 4e shows the spectrum of losses ( $\alpha_{\text{film}}$ ) for UV-visible light passing through such a reference film. These data allow one to estimate the losses due to MoS<sub>2</sub> self-absorption and bulk scattering at the peak emission wavelength (about 550 nm) to be about  $70 \text{ cm}^{-1}$ . Additional waveguiding losses directly related to the structure and defects of MoS<sub>2</sub>-polymer filaments are therefore limited to a few tens of  $\text{cm}^{-1}$ . This further demonstrates that these fibers are uniform and free of defects and

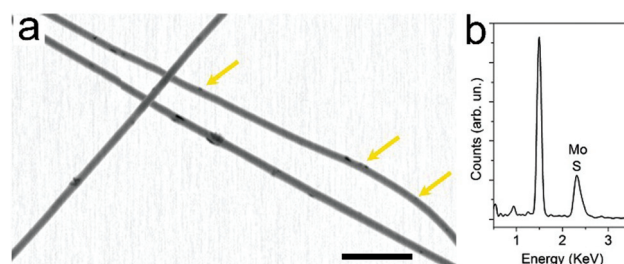


**Fig. 5** (a) STEM micrograph of hybrid nanofibers. Interspersed particles and aggregates are clearly visible (some are highlighted by yellow arrows). Scale bar = 10 μm. The corresponding EDS profile is shown in (b). The peak at 1.5 keV corresponds to aluminum in the foil used as a collector for fiber deposition.



suggests that they are highly promising building blocks for optical circuits and ports.

For instance, light scattering from inhomogeneities along the fiber axis could be promoted by clusters of particles, as indicated by the bright spots shown in Fig. 4c and d. The typical distance between consecutive light-scattering spots in the  $\mu$ -PL micrographs is indeed of a few  $\mu\text{m}$ , which agrees well with the inter-cluster distance determined by the STEM imaging of the hybrid fibers (Fig. 5).

## 4. Conclusions

In conclusion, we produced  $\text{MoS}_2$  NPs with a simple and inexpensive ultrasonication process and realized hybrid fibers based on these NPs. The exfoliation strategy reduces the  $\text{MoS}_2$  powder size in all three spatial dimensions while preserving the low defect concentration and homogeneity in terms of sulphur stoichiometry.  $\text{MoS}_2$  is then homogeneously encapsulated in electrospun polymer filaments, which are smooth and uniform and show photonic functionality (*i.e.*, waveguiding capability of the self-emitted light along the longitudinal fiber axis). The advantages of hybrid photonic systems based on  $\text{MoS}_2$  over light-emitting nanocomposites embedded with well-established semiconducting quantum dots might be numerous, particularly in terms of excitation-dependent emission features and low cytotoxicity,<sup>52</sup> making them interesting for use in biomedical applications including endoscopy and optogenetics. Furthermore, the large surfaces of these dopants can be bio-functionalized through different routes,<sup>53,54</sup> thus opening perspectives for use in diagnostic labs-on-a-chip and miniaturized chemical and optical biosensors.<sup>55</sup> Finally, the light transport along these  $\text{MoS}_2$ -polymer fibers is efficient over distances of many tens of  $\mu\text{m}$ . As they enable photon channeling over length scales typical of photonic chips,  $\text{MoS}_2$ -polymer fibers might find applications in quantum technologies.<sup>50</sup> By providing electromagnetic field confinement, the fibers can be exploited for the optical detection of field-interacting chemical species placed near the waveguide. The fibers can also be used for coupling radiation to other active nanomaterials through the evanescent field at their surface. All these aspects make these novel optical materials highly interesting for integration in complex, system-level platforms for sensing and in flexible optoelectronics.

## Conflicts of interest

There are no conflicts to declare.

## Acknowledgements

The research leading to these results has received funding from the European Research Council under the European Union's Seventh Framework Programme (FP/2007-2013)/ERC Grant Agreement no. 306357 (ERC Starting Grant

"NANO-JETS"). D. P. also acknowledges the support from the project PRA\_2018\_34 ("ANISE") from the University of Pisa.

## References

- 1 K. F. Mak, C. Lee, J. Hone, J. Shan and T. F. Heinz, *Phys. Rev. Lett.*, 2010, **105**, 136805.
- 2 Q. H. Wang, K. Kalantar-Zadeh, A. Kis, J. N. Coleman and M. S. Strano, *Nat. Nanotechnol.*, 2012, **7**, 699.
- 3 B. W. Baugher, H. O. Churchill, Y. Yang and P. Jarillo-Herrero, *Nano Lett.*, 2013, **13**, 4212.
- 4 W. Zhu, T. Low, Y. H. Lee, H. Wang, D. B. Farmer, J. Kong, F. Xia and P. Avouris, *Nat. Commun.*, 2014, **5**, 3087.
- 5 B. Radisavljevic, A. Radenovic, J. Brivio, V. Giacometti and A. Kis, *Nat. Nanotechnol.*, 2011, **6**, 147.
- 6 A. Splendiani, L. Sun, Y. Zhang, T. Li, J. Kim, C. Y. Chim, G. Galli and F. Wang, *Nano Lett.*, 2010, **10**, 1271.
- 7 S. Mukherjee, R. Maiti, A. Midya, S. Das and S. K. Ray, *ACS Photonics*, 2015, **2**, 760.
- 8 H. Hwang, H. Kim and J. Cho, *Nano Lett.*, 2011, **11**, 4826.
- 9 U. K. Sen and S. Mitra, *ACS Appl. Mater. Interfaces*, 2013, **5**, 1240.
- 10 D. Gopalakrishnan, D. Damien and M. M. Shaijumon, *ACS Nano*, 2014, **8**, 5297.
- 11 J. Y. Wu, X. Y. Zhang, X. D. Ma, Y. P. Qiu and T. Zhang, *RSC Adv.*, 2015, **5**, 95178.
- 12 C. L. Zhang and S. H. Yu, *Chem. Soc. Rev.*, 2014, **43**, 4423.
- 13 S. Y. Min, J. Bang, J. Park, C. L. Lee, S. Lee, J. J. Park, U. Jeong, S. Kim and T. W. Lee, *RSC Adv.*, 2014, **4**, 11585.
- 14 Y. Lee, J. Y. Oh, T. R. Kim, X. Gu, Y. Kim, G. J. N. Wang, H. C. Wu, R. Pfattner, J. W. F. To, T. Katsumata, D. Son, J. Kang, J. R. Matthews, W. J. Niu, M. Q. He, R. Sinclair, Y. Cui, J. B. H. Tok, T. W. Lee, Z. N. Bao and D. Son, *Adv. Mater.*, 2018, **30**, 1704401.
- 15 Y. Lee, S. Y. Min and T. W. Lee, *Macromol. Mater. Eng.*, 2017, **302**, 1600507.
- 16 D. H. Reneker and I. Chun, *Nanotechnology*, 1996, **7**, 216.
- 17 A. Greiner and J. H. Wendorff, *Angew. Chem., Int. Ed.*, 2007, **46**, 5670.
- 18 L. Persano, A. Camposeo and D. Pisignano, *Prog. Polym. Sci.*, 2015, **43**, 48.
- 19 S. Y. Min, T. S. Kim, B. J. Kim, H. Cho, Y. Y. Noh, H. Yang, J. H. Cho and T. W. Lee, *Nat. Commun.*, 2013, **4**, 1773.
- 20 W. Xu, S. Y. Min, H. Hwang and T. W. Lee, *Sci. Adv.*, 2016, **2**, e1501326.
- 21 M. V. Kakade, S. Givens, K. Gardner, K. H. Lee, D. B. Chase and J. F. Rabolt, *J. Am. Chem. Soc.*, 2007, **129**, 2777.
- 22 S. Pagliara, M. S. Vitiello, A. Camposeo, A. Polini, R. Cingolani, G. Scamarcio and D. Pisignano, *J. Phys. Chem. C*, 2011, **115**, 20399.
- 23 M. Richard-Lacroix and C. Pellerin, *Macromolecules*, 2013, **46**, 9473.



- 24 L. Persano, A. Camposeo, A. V. Terentjevs, F. Della Sala, E. Fabiano, M. Montinaro and D. Pisignano, *Adv. Mater.*, 2017, **29**, 1701031.
- 25 X. Xiong, W. Luo, X. Hu, C. Chen, L. Qie, D. Hou and Y. Huang, *Sci. Rep.*, 2015, **5**, 9254.
- 26 C. Zhao, J. Kong, X. Yao, X. Tang, Y. Dong, S. L. Phua and X. Lu, *ACS Appl. Mater. Interfaces*, 2014, **6**, 6392.
- 27 A. O'Neill, U. Khan and J. N. Coleman, *Chem. Mater.*, 2012, **24**, 2414.
- 28 Y. Yao, L. Tolentino, Z. Yang, X. Song, W. Zhang, Y. Chen and C. P. Wong, *Adv. Funct. Mater.*, 2013, **23**, 3577.
- 29 A. P. Gaur, S. Sahoo, M. Ahmadi, S. P. Dash, M. J. F. Guinel and R. S. Katiyar, *Nano Lett.*, 2014, **14**, 4314.
- 30 A. Jawaid, D. Nepal, K. Park, M. Jespersen, A. Qualley, P. Mirau, L. F. Drummy and R. A. Vaia, *Chem. Mater.*, 2015, **28**, 337.
- 31 L. Zhang, W. Fan, W. W. Tjiu and T. Liu, *RSC Adv.*, 2015, **5**, 34777.
- 32 D. Zhang, J. Wu, P. Li and Y. Cao, *J. Mater. Chem. A*, 2017, **5**, 20666.
- 33 V. Štengl and J. Henych, *Nanoscale*, 2013, **5**, 3387.
- 34 J. N. Coleman, M. Lotya, A. O'Neill, S. D. Bergin, P. J. King, U. Khan, K. Young, A. Gaucher, S. De, R. J. Smith, I. V. Shvets, S. K. Arora, G. Stanton, H. Y. Kim, K. Lee, G. T. Kim, G. S. Duesberg, T. Hallam, J. J. Boland, J. J. Wang, J. F. Donegan, J. C. Grunlan, G. Moriarty, A. Shmeliov, R. J. Nicholls, J. M. Perkins, E. M. Grievson, K. Theuwissen, D. W. McComb, P. D. Nellist and V. Nicolosi, *Science*, 2011, **331**, 568.
- 35 T. Cheiwchanchamnangij and W. R. Lambrecht, *Phys. Rev. B: Condens. Matter Mater. Phys.*, 2012, **85**, 205302.
- 36 R. A. Bromley, R. B. Murray and A. D. Yoffe, *J. Phys. C: Solid State Phys.*, 1972, **5**, 759.
- 37 A. R. Beal, J. C. Knights and W. Y. Liang, *J. Phys. C: Solid State Phys.*, 1972, **5**, 3540.
- 38 K. Wang, J. Wang, J. Fan, M. Lotya, A. O'Neill, D. Fox, Y. Feng, X. Zhang, B. Jiang, Q. Zhao, H. Zhang, J. N. Coleman, L. Zhang and W. J. Blau, *ACS Nano*, 2013, **7**, 9260.
- 39 W. Qiao, S. Yan, X. He, X. Song, Z. Li, X. Zhang, W. Zhong and Y. Du, *RSC Adv.*, 2014, **4**, 50981.
- 40 C. Lee, H. Yan, L. E. Brus, T. F. Heinz, J. Hone and S. Ryu, *ACS Nano*, 2010, **4**, 2695.
- 41 H. Li, Q. Zhang, C. C. R. Yap, B. K. Tay, T. H. T. Edwin, A. Olivier and D. Baillargeat, *Adv. Funct. Mater.*, 2012, **22**, 1385.
- 42 W. M. Parkin, A. Balan, L. Liang, P. M. Das, M. Lamparski, C. H. Naylor, J. A. Rodríguez-Manzo, A. T. C. Johnson, V. Meunier and M. Drndić, *ACS Nano*, 2016, **10**, 4134.
- 43 F. Fabbri, E. Rotunno, E. Cinquanta, D. Campi, E. Bonnini, D. Kaplan, L. Lazzarini, M. Bernasconi, C. Ferrari, M. Longo, G. Nicotra, A. Molle, V. Swaminathan and G. Salviati, *Nat. Commun.*, 2016, **7**, 13044.
- 44 C. Backes, R. J. Smith, N. McEvoy, N. C. Berner, D. McCloskey, H. C. Nerl, A. O'Neill, P. J. King, T. Higgins, D. Hanlon, N. Scheuschner, J. Maultzsch, L. Houben, G. S. Duesberg, J. F. Donegan, V. Nicolosi and N. Scheuschner, *Nat. Commun.*, 2014, **5**, 4576.
- 45 S. Mukherjee, R. Maiti, A. K. Katiyar, S. Das and S. K. Ray, *Sci. Rep.*, 2016, **6**, 29016.
- 46 W. Dai, H. Dong, B. Fugetsu, Y. Cao, H. Lu, X. Ma and X. Zhang, *Small*, 2015, **11**, 4158.
- 47 H. Dong, S. Tang, Y. Hao, H. Yu, W. Dai, G. Zhao, Y. Cao, H. Lu, X. Zhang and H. Ju, *ACS Appl. Mater. Interfaces*, 2016, **8**, 3107.
- 48 M. Moffa, V. Fasano, A. Camposeo, L. Persano and D. Pisignano, *Proc. SPIE*, 2016, **9745**, 97450S.
- 49 V. Fasano, A. Polini, G. Morello, M. Moffa, A. Camposeo and D. Pisignano, *Macromolecules*, 2013, **46**, 5935.
- 50 M. Gaio, M. Moffa, M. Castro-Lopez, D. Pisignano, A. Camposeo and R. Sapienza, *ACS Nano*, 2016, **10**, 6125.
- 51 T. Kaino and Y. Katayama, *Polym. Eng. Sci.*, 1989, **29**, 1209.
- 52 J. H. Appel, D. O. Li, J. D. Podlevsky, A. Debnath, A. A. Green, Q. H. Wang and J. Chae, *ACS Biomater. Sci. Eng.*, 2016, **2**, 361.
- 53 D. Voiry, A. Goswami, R. Kappera, C. de Carvalho Castro e Silva, D. Kaplan, T. Fujita, M. Chen, T. Asefa and M. Chhowalla, *Nat. Chem.*, 2015, **7**, 45.
- 54 R. M. Kong, L. Ding, Z. Wang, J. You and F. Qu, *Anal. Bioanal. Chem.*, 2015, **407**, 369.
- 55 S. Barua, H. S. Dutta, S. Gogoi, R. Devi and R. Khan, *ACS Appl. Nano Mater.*, 2018, **1**, 2.

